

A Novel Approach for Defect Detection on Vessel Structures using Saliency-related Features

Francisco Bonnin-Pascual^{a,*}, Alberto Ortiz^a

^a*Department of Mathematics and Computer Science, University of the Balearic Islands,
Cra. Valldemossa km 7.5, 07122 Palma de Mallorca, Spain*

Abstract

Seagoing vessels have to undergo regular visual inspections in order to detect defects such as cracks and corrosion before they result into catastrophic consequences. These inspections are currently performed manually by ship surveyors at a great cost, so that any level of assistance during the inspection process by means of e.g. a fleet of robots capable of defect detection would significantly decrease the inspection cost. In this paper, we describe a novel framework for visually detecting the aforementioned defects. This framework is generic and flexible in the sense that it can be easily configured to compute the features that perform better for the inspection at hand. Making use of this framework and inspired by the idea of conspicuity, this work considers contrast and symmetry as features for detecting defects and shows their usefulness for the case of vessels. Three different combination operators are additionally tested in order to merge the information provided by these features and improve the detection performance. Experimental results for different configurations of the detection framework show better classification rates than state of the art methods and prove its usability for images collected by a micro-aerial robotic platform intended for vessel visual inspection.

Keywords:

Defect detection, Vessel inspection, Corrosion, Cracks, Saliency, Micro-Aerial Vehicle

*Corresponding author: Tel.: +34-971-172-565;
Email address: xisco.bonnin@uib.es (Francisco Bonnin-Pascual)

1 1. Introduction

2 Vessels are nowadays one of the most cost effective ways to transport
3 goods around the world. Despite the efforts to avoid maritime accidents
4 and wreckages, these still occur, and, from time to time, have catastrophic
5 consequences in environmental, human and/or economic terms. Structural
6 failures are the main cause of these accidents and, as such, Classification So-
7 cieties impose extensive inspection schemes in order to ensure the structural
8 integrity of vessels.

9 An important part of the vessel maintenance has to do with the visual
10 inspection of the internal and external parts of the vessel hull. They can be
11 affected by different kinds of defects typical of steel surfaces and structures,
12 such as cracks and corrosion. These defects are indicators of the state of the
13 metallic surface and, as such, an early detection prevents the structure from
14 buckling and/or fracturing.

15 To carry out this task, the vessel has to be emptied and situated in a
16 dockyard where high scaffoldings are installed to allow the human inspectors
17 to access the highest parts of the vessel structure (more than 30 m high).
18 Taking into account the huge dimensions of some vessels, this process can
19 mean the visual assessment of more than 600,000 m² of steel. Besides, the
20 surveys are on many occasions performed in hazardous environments for
21 which the access is usually difficult and the operational conditions turn out
22 to be sometimes extreme for human operation. Moreover, total expenses
23 involved by the infrastructure needed for close-up inspection of the hull can
24 reach up to one million dollars for certain sorts of vessels (e.g. Ultra Large
25 Crude Carriers). Therefore, it is clear that any level of automation of the
26 inspection process that can lead to a reduction of the inspection time, a
27 reduction of the financial costs involved and/or an increase in the safety of
28 the operation is fully justified.

29 The European projects MINOAS (finished on 2012) and INCASS (in de-
30 velopment until 2016) have among their goals the development of robotic
31 platforms to automate as much as possible the inspection process of vessels
32 (Eich et al., 2014). One of these robots is a micro-aerial vehicle fitted with
33 cameras, which is in charge of collecting images that can provide the sur-
34 veyor with a global overview of the different surfaces and structures of the
35 inspected vessel (Bonnin-Pascual et al., 2015). These images are intended to
36 be processed afterwards to autonomously detect the defective areas. Regard-
37 ing the latter, this paper presents a novel approach for automatic detection

38 of defects in images taken from the vessel structures. A framework is pro-
39 posed as a generic classifier that can be configured to make use of different
40 features, potentially leading to different defect detectors each. Furthermore,
41 the framework foresees the combination of the respective feature responses in
42 order to enhance the overall output quality. The conspicuousness of defects
43 in general, together with the kind of defects that can be expected in metallic
44 surfaces (i.e. cracks and corrosion) and the image capture conditions, have
45 guided the feature selection process.

46 Previous approaches on vision-based defect detection can be roughly clas-
47 sified into two big categories. On the one hand, there are lots of contributions
48 on industrial inspection and quality control; that is to say, algorithms that
49 are in charge of checking whether the products that result from an industrial
50 manufacturing process are in good condition. These methods assume a more
51 or less confined environment where the product to be inspected is always
52 situated in a similar position, while lighting conditions are controlled as well.
53 Most of these techniques are collected in Chin and Harlow (1982); Newman
54 (1995); Malamas et al. (2003); Xie (2008).

55 On the other hand, several other contributions focus on visual inspection
56 techniques to ensure the integrity of elements or structures that have been
57 subjected to some kind of effort or stress. These methods are typically in-
58 cluded in periodical surveys to assess the need of maintenance operations. In
59 this group, which include vessel hull inspection, we can find algorithms for
60 crack detection on concrete surfaces (Yamaguchi and Hashimoto, 2010), de-
61 fect detection on bridge structures (Jahanshahi et al., 2009), aircraft surface
62 inspection (Siegel and Gunatilake, 1998; Mumtaz et al., 2010), etc.

63 The majority of the algorithms from both categories have been devised
64 for the detection of a specific defect on a particular material or surface, while
65 much less methods deal with unspecified defects on general surfaces. The
66 short distance from which the images must be captured is another point in
67 common among the majority of the algorithms. Furthermore, to provide
68 good results, most of them require from a learning stage and/or tuning their
69 operating parameters.

70 Regarding defect detection over vessel structures, just a few contribu-
71 tions can be found. For example, Ozog and Eustice (2015) present a method
72 to identify structural anomalies over image reconstructions of underwater
73 ship hulls. Restricting to those contributions which use just visual sensors,
74 Bonnin-Pascual (2010) and Bonnin-Pascual and Ortiz (2014b) present de-
75 tectors of cracks and corrosion for vessel structures. These algorithms do

76 not need close-up images of the inspected surfaces to provide good results
77 but their drawback is again that they require a previous training stage (e.g.
78 to learn which is the color that corrosion usually presents) or tuning their
79 working parameters (e.g. to know how thin and elongated must be a dark
80 collection of pixels to be considered as a crack), whose value is typically
81 related with the distance from which the images have been collected.

82 To the best of our knowledge, only one method has been published for
83 generic defect detection in vessel structure images (Bonnin-Pascual and Or-
84 tiz, 2014a). This approach makes use of a Bayesian framework to compute
85 the probability for every pixel of corresponding to some kind of defective
86 situation. This probability is based on the information learned in a previous
87 training stage.

88 The rest of the paper is organized as follows: Section 2 describes the
89 generic flexible defect detection framework; Section 3 explains how this frame-
90 work particularizes for defect detection in vessel structures, considering con-
91 trast (3.1), symmetry (3.2) and three alternative combinations among them
92 (3.3); Section 4 discuss on the results of some experiments; and Section 5
93 concludes the paper.

94 **2. A Flexible Framework for Defect Detection**

95 The importance of feature selection during the design of any vision-based
96 classifier is discussed in Theodoridis and Koutroumbas (2006). In particular,
97 the following questions must be answered: (1) which features are the best for
98 a suitable classification, (2) how many features are necessary, and (3) how
99 should these be combined to implement the best classifier.

100 Taking that into account, we oriented the design of our defect detector
101 towards a flexible framework which allows an easy integration of different
102 features and their combinations. To attain this level of flexibility, we consid-
103 ered that the framework must cover the following aspects: (1) it should allow
104 computing one or more features that are potentially useful to discriminate
105 between defective and non-defective situations; (2) final features response
106 should not depend on scale; (3) one or more combination operators should
107 be available to merge the information provided by the computed features
108 and try to find the combination (if any) that improves the classification per-
109 formance; and (4) related to the previous point, one or more normalization
110 operators should be available to adapt the different features responses to a
111 certain range, in order to prevent loosing information when combining them.

112 This generic framework has been implemented as a modular pipeline
113 which involves different stages that can be configured (or even removed)
114 depending on our needs, so that different configurations result into different
115 defect detectors (see Fig. 1). Within the framework, each feature is intended
116 to be computed as a different thread and the information that they all provide
117 can be finally combined to make up the detection output.

118 In more detail, the framework consists of the following stages:

- 119 • *Pre-feature computation.* The first stage prepares the input image to
120 provide the information necessary to compute all features. From an
121 input color image one can obtain, for example, the gray-scale (or inten-
122 sity) image, the red channel image, the saturation image (from HSV
123 color space), etc. Each one of these images is called a *pre-feature map*.
- 124 • *Scale-space generation.* This stage scales the pre-feature maps using a
125 range of scale factors to obtain a collection of multiple-scale representa-
126 tions, also known as pyramids. The computation of each pyramid level
127 can include filtering the input map using some kind of filter. One can
128 compute, for example, a Gaussian pyramid which progressively low-
129 pass filters and sub-samples the pre-feature map, an oriented Gabor
130 pyramid for a preferred orientation θ , a simple sub-sampled pyramid
131 computed without any filtering, etc.
- 132 • *Feature computation.* This is the core stage within the pipeline. Each
133 instance of this stage is in charge of computing the value for a given
134 feature for all the pixels of the input image. Since this can be fed with
135 one or more multi-scale pyramids, a feature can be computed combining
136 the information provided at different scales. Each output of this stage
137 is called a *feature map*.
- 138 • *Normalization.* It normalizes the different feature maps to the same
139 range of values to enable their combination.
- 140 • *Combination.* This is the last stage of the pipeline. It is in charge of
141 combining the normalized feature maps in order to obtain a single map,
142 which is called the *defect map*. The mean and the median operators
143 are some examples of simple combination operators. Unary operators
144 such as unary minus or thresholding can be also considered.

145 As indicated in Fig. 1, the generic framework allows computing more complex
146 features by means of concatenating multiple instances of normalization
147 and combination stages.

148 The output of the framework is the defect map, which consists in a single-
149 channel map where defective areas are supposed to be labelled with higher
150 values.

151 3. Detecting Defects on Vessel Structures

152 Vessel structures consist of large surfaces that usually present a regular
153 texture. When these surfaces are inspected from a certain distance, a defect
154 represents a discontinuity that alters the regularity of the texture. Based
155 on that, texture-related features seem to be a good option to differentiate
156 between defective and non-defective areas.

157 Furthermore, defects can also be considered as rare phenomena that may
158 appear on such regular surfaces. Since they are rare, defects potentially
159 attract the visual attention of the surveyor during a visual inspection process.
160 Following these ideas, we propose to use texture-based features typically used
161 in cognitive models to predict human eye fixations.

162 Among them, we focus on those which can be evaluated through a saliency
163 map. A saliency map consists in a topographic map that represents the
164 conspicuousness of the different areas of the input image (Koch and Ullman,
165 1985). This is typically shown as a gray-scale image where locations with
166 higher conspicuity values are closer to white and less salient areas are closer
167 to black. Notice that this representation fits with our definition of defect
168 map.

169 Taking all these considerations into account, contrast and symmetry have
170 been selected as the features for detecting defects on vessel structures. The
171 following sections detail further about the motivations that led us to consider
172 these features as well as describe how the defect detector makes use of them.

173 3.1. The Contrast-based Defect Detector

174 As indicated in Borji and Itti (2013), three features have been traditionally
175 used in computational models of attention: intensity, color and orientation.
176 The sudden variation of some of these features, computed as a local
177 contrast, increases the conspicuousness of the area producing bottom-up
178 guidance (Wolfe, 2007).

179 The information resulting from the variation of these three features is
 180 typically combined into a single contrast-based saliency map. See for example
 181 Avraham and Lindenbaum (2010); Borji et al. (2011); Li et al. (2010); Zhang
 182 et al. (2015).

183 We propose to use this local contrast (combining intensity, color and ori-
 184 entation) in a first attempt to locate corrosion and cracks on vessel structures.

185 The generic framework described in section 2 is of application now to
 186 design the contrast-based defect detector. The model presented in Itti et al.
 187 (1998) has been used as source of inspiration to design the different stages of
 188 the pipeline. The previous work described for the first time a contrast-based
 189 model for saliency and has inspired later authors (Borji and Itti, 2013).

190 Figure 3 details the contrast-based defect detector. As for its imple-
 191 mentation, each one of the stages of the generic pipeline (Fig. 1) has been
 192 particularized as follows:

- 193 • *Pre-feature computation.* Five pre-feature maps are computed from the
 194 red (r), green (g) and blue (b) channels of the input image:

$$I = \frac{r + g + b}{3}, \quad (1)$$

$$R = r - \frac{g + b}{2}, \quad (2)$$

$$G = g - \frac{r + b}{2}, \quad (3)$$

$$B = b - \frac{r - g}{2}, \quad (4)$$

$$Y = \frac{r + g}{2} - \frac{|r - g|}{2} - b, \quad (5)$$

199 where I is an intensity map, R is a red channel map, G is a green
 200 channel map, B is a blue channel map and Y is a yellow channel map.
 201 During the computation of these maps, negative values (if any) are set
 202 to zero.

- 203 • *Scale-space generation.* Nine pyramids are computed from the pre-
 204 feature maps. On the one hand, five Gaussian pyramids \hat{I} , \hat{R} , \hat{G} , \hat{B} and
 205 \hat{Y} are computed by progressively low-pass filtering and sub-sampling

the pre-feature maps (I , R , G , B and Y). On the other hand, four Gabor pyramids \widehat{O}_0 , \widehat{O}_{45} , \widehat{O}_{90} and \widehat{O}_{135} are computed filtering the images of the intensity pyramid \widehat{I} with oriented Gabor filters with orientations $\theta \in \{0^\circ, 45^\circ, 90^\circ, 135^\circ\}$. All pyramids comprise seven scales, ranging from 1:1 (scale one) to 1:64 (scale seven).

- *Feature computation.* Three threads are executed in parallel to build three feature maps, respectively corresponding to the contrast level in intensity (\mathbf{I}), color (\mathbf{C}) and orientation (\mathbf{O}). This computation is performed as indicated in Itti et al. (1998). A first step computes center-surround differences between fine and coarse scales from the pyramids; that is, it computes the difference between each pixel of a fine (or center) scale c and its corresponding pixel in a coarse (or surrounding) scale s . Accordingly, preliminary maps $\mathbf{I}(c, s)$, $\mathbf{RG}(c, s)$, $\mathbf{BY}(c, s)$ and $\mathbf{O}(c, s, \theta)$ are created as follows:

$$\mathbf{I}(c, s) = |I(c) \ominus I(s)|, \quad (6)$$

$$\mathbf{RG}(c, s) = |R(c) - G(c)) \ominus (G(s) - R(s))|, \quad (7)$$

$$\mathbf{BY}(c, s) = |(B(c) - Y(c)) \ominus (Y(s) - B(s))|, \quad (8)$$

$$\mathbf{O}(c, s, \theta) = |O(c, \theta) \ominus O(s, \theta)|, \quad (9)$$

where $|x|$ refers to the absolute value of x , \ominus is the across-scale subtraction operator (see Fig. 2), $\mathbf{I}(c, s)$ accounts for the intensity contrast, $\mathbf{RG}(c, s)$ accounts for red/green contrast, $\mathbf{BY}(c, s)$ accounts for blue/yellow contrast and $\mathbf{O}(c, s, \theta)$ accounts for the orientation contrast for a given orientation θ . In our implementation the scales are defined as $c \in \{1, 2, 3\}$ and $s = c + \delta$, with $\delta \in \{3, 4\}$.

In a second step, the intermediate maps are combined into the three feature maps by means of the across-scale addition operator \oplus (see Fig. 2 for details):

$$\mathbf{I} = \bigoplus_{c=1}^3 \bigoplus_{s=c+3}^{c+4} N(\mathbf{I}(c, s)), \quad (10)$$

$$\mathbf{C} = \bigoplus_{c=1}^3 \bigoplus_{s=c+3}^{c+4} (N(\mathbf{RG}(c, s)) + N(\mathbf{BY}(c, s))), \quad (11)$$

$$\mathbf{O} = \sum_{\theta \in \{0^\circ, 45^\circ, 90^\circ, 135^\circ\}} N \left(\bigoplus_{c=1}^3 \bigoplus_{s=c+3}^{c+4} N(\mathbf{O}(c, s, \theta)) \right), \quad (12)$$

where $N(\cdot)$ is a normalization operator devised to promote high and isolated peaks. It consists in adjusting the map to a fixed range $[0..M]$ and multiplying it by $(M - \bar{m})^2$, being \bar{m} the average of all local maxima that do not coincide with the global maximum.

By way of illustration, a diagram showing the entire feature computation for map \mathbf{I} can be found in Fig. 2.

- *Normalization.* The normalization operator $N(\cdot)$ is used now to promote the highest and isolated peaks in the three feature maps, obtaining $\bar{\mathbf{I}}$ for intensity, $\bar{\mathbf{C}}$ for color and $\bar{\mathbf{O}}$ for orientation.
- *Combination.* The final defect map is computed using the linear combination:

$$\mathbf{D}_{con} = \frac{\bar{\mathbf{I}} + \bar{\mathbf{C}} + \bar{\mathbf{O}}}{3}, \quad (13)$$

so that any salient point in any of the feature maps appears in the final defect map.

3.2. The Symmetry-based Defect Detector

A saliency model based on the Gestalt principle of symmetry was presented in Kootstra et al. (2008). In their paper, they discuss local symmetry as a measure of saliency and investigate its role in visual attention. To this end, they use three different symmetry operators (isotropic, radial and color symmetry operators) and compare them with human eye tracking data. The results suggest that symmetry is a salient structural feature for humans, as well as the suitability of their method for predicting human eye fixations in complex photographic images, where symmetry is not so evident.

Furthermore, the authors use the saliency model by Itti et al. as a reference for comparison. Their results show that, on many occasions, their symmetry operators outperform the contrast-saliency model.

257 For all these reasons, symmetry is the second feature that has been
 258 selected for this study. Figure 4 shows our implementation of the symmetry-
 259 based defect detector using the generic framework (Fig. 1), where each stage
 260 is particularized as follows:

- 261 • *Pre-feature computation.* It just computes one intensity map as indicated in Eq. 1.
- 263 • *Scale-space generation.* This stage computes a simple sub-sample pyramid with five scales, ranging from 1:1 (scale one) to 1:16 (scale five).
- 265 • *Feature computation.* The symmetry map is computed for each level l of the pyramid, using the isotropic operator. We have chosen this operator because it is easier to compute and no significant improvement was observed when using the radial or color symmetry operators for predicting human eye fixations (Kootstra and Schomaker, 2009).

270 To obtain the final defect map based on symmetry, the five responses
 271 $\mathbf{M}(l)$ (one per pyramid level) are normalized using the normalization
 272 operator $N(\cdot)$ and finally added together across-scale into an scale 1:1
 273 map:

$$\mathbf{D}_{sym} = \bigoplus_{l=1}^5 N(\mathbf{M}(l)). \quad (14)$$

274 Normalization and combination stages are not employed for this case since
 275 symmetry is the only feature used.

276 3.3. Combination of Contrast and Symmetry

277 In order to deeper explore the possibilities of the selected features, the
 278 generic framework has been configured to combine the information that they
 279 convey in the following way:

- 280 • *Pre-feature computation.* Five pre-feature maps are computed as described for contrast-based method.
- 282 • *Scale-space generation.* It generates ten pyramids, nine used for contrast plus one used for symmetry, as detailed in, respectively, sections
 283 3.1 and 3.2.

- 285 ● *Feature computation.* It consists of four threads, one for each channel of
 286 contrast (intensity, color and orientation) plus one for symmetry. They
 287 proceed as indicated in previous sections.
- 288 ● *Normalization.* The normalization operator $N(\cdot)$ of section 3.1 is used
 289 in this stage to promote the areas from the feature maps that have been
 290 indicated as potentially defective by any of the features. Therefore,
 291 $\overline{\mathbf{D}_{con}}$ is obtained as the normalized version of the defect map based on
 292 contrast and $\overline{\mathbf{D}_{sym}}$ is the analogue for the case of symmetry.
- 293 ● *Combination.* We initially propose two operators. The first one con-
 294 sists in a linear combination of the contrast and symmetry-based defect
 295 maps:

$$\mathbf{D}_{OR} = \frac{\overline{\mathbf{D}_{con}} + \overline{\mathbf{D}_{sym}}}{2}. \quad (15)$$

296 This combination allows any defective point in any of the maps to be
 297 promoted so that it stands out in the final defective map. It will be
 298 referred to as the *OR* combination.

299 The second combination operator that we propose merges the contrast
 300 and symmetry-based defect maps so that defective regions in the re-
 301 sulting map are required to be simultaneously indicated as potentially
 302 defective in both maps, implementing, in a certain sense, the logical
 303 *AND* operator:

$$\mathbf{D}_{AND} = \overline{\mathbf{D}_{con}} \times \overline{\mathbf{D}_{sym}}. \quad (16)$$

304 In addition to these combinations, a third version has been considered
 305 which intends to explore the contribution provided by the different
 306 contrast channels, i.e., intensity, color and orientation. The four feature
 307 maps (including the symmetry map) are fused using a modified version
 308 of the OR combination, which will be referred to as the *ORA* (Or-
 309 Alternative) combination:

$$\mathbf{D}_{ORA} = \frac{\overline{\mathbf{I}} + \overline{\mathbf{C}} + \overline{\mathbf{O}} + \overline{\mathbf{D}_{sym}}}{4}. \quad (17)$$

310 Figure 5 shows the set up of the normalization and combination stages
 311 for the three detectors which combine contrast and symmetry information.

312 **4. Assessment of the Defect Detector**

313 In this study, we have used a dataset comprising 73 images of vessel
314 structures including defective areas (cracks, coating breakdown and different
315 kinds of corrosion). The images have been collected at different distances
316 and at different lighting conditions. This dataset is available online (<http://dmi.uib.es/~xbonnin/resources>) and also includes the ground truth,
317 consisting in black and white images where defects are labelled in white (see
318 Fig. 7:B).

320 In a first kind of experiment, we have assessed the suitability of using
321 contrast and symmetry to differentiate between defective and non-defective
322 areas. To this end, the probability distribution of these two features has
323 been computed for the two classes, defective and non-defective area. To es-
324 timate these PDFs, we have applied the Parzen windows method (Theodor-
325 idis and Koutroumbas, 2006) to the histograms computed for combinations
326 contrast/defect, symmetry/defect, contrast/non-defect and symmetry/non-
327 defect. The resulting PDFs are shown in Fig. 6. We can state the following
328 looking at those PDFs:

- 329 • non-defective pixels present low values of contrast and symmetry (below
330 10 for contrast and around 15 for symmetry), what confirms that non-
331 defective areas present a more or less homogeneous texture.
- 332 • defective pixels tend to present higher values of both features (around
333 25), so that this features seem to be useful to differentiate between
334 defective and non-defective areas.
- 335 • contrast peaks are farther from each other than symmetry peaks, what
336 could indicate that contrast is more discriminative than symmetry
337 when describing the defective areas that appear in our dataset.

338 In a second kind of experiments, we evaluated the performance of the
339 proposed defect detectors. Figure 7 presents some examples of defect maps
340 provided for the different cases, namely, the contrast-based detector, the
341 symmetry-based one and the three detectors which combine these two fea-
342 tures using, respectively, the OR, AND and ORA combination operators.

343 At first sight, it can be observed that all the defect detectors tend to label
344 in lighter gray the areas that are indicated as defective in the ground truth
345 image. This suggests that the different detectors can attain good classifica-
346 tion rates.

347 In order to perform a quantitative evaluation, the True Positive Rate
348 (TPR), or sensitivity, and the False Positive Rate (FPR), or fall-out, have
349 been computed for the five defect detectors. To this end, the defect maps were
350 thresholded for different values of a threshold τ to obtain the corresponding
351 ROC curves, which are presented in Fig. 8. Furthermore, to complete the
352 assessment, the values for the Area Under the Curve (AUC) (Fawcett, 2006)
353 have been calculated for all the ROC curves, obtaining the values also shown
354 in Fig. 8.

355 Comparing the different ROC curves and AUC values, some interesting
356 results can be stated: (1) the five defect detectors present good performances
357 during the classification task, with ROC curves relatively close to the (0,1)
358 corner (corresponding to the perfect classifier), and AUC values above 0.8;
359 (2) contrast performs better than symmetry for the dataset employed in this
360 study, what suggests that contrast provides more information to discriminate
361 between defective and non-defective areas in vessel structures; (3) the three
362 detectors which combine both contrast and symmetry information provide
363 slightly better results than the version based only on contrast (i.e. symmetry
364 provides complementary information), being the ORA combination the one
365 which yields the highest AUC value.

366 In a third kind of experiments, the performances of the defect detectors
367 presented in this paper have been compared with the one attained by some
368 state of the art defect detectors. Each comparative assessment is performed
369 using ROC curves, which are provided in separate figures to simplify their
370 interpretation. In a first experiment, we have compared with the WCCD
371 algorithm (Bonnin-Pascual, 2010). This algorithm was devised for corrosion
372 detection in images taken from vessel structures. It consists in a cascade
373 classifier that combines texture (described as the energy of a gray-level co-
374 occurrence matrix downsampled to 32×32) and colour information, and has
375 proved to outperform other more complex weak-classifier combinations, such
376 as the ABCD algorithm (Bonnin-Pascual and Ortiz, 2014b), which combines
377 Laws' texture energy filters within an AdaBoost framework. Notice that
378 both WCCD and ABCD follow a supervised classification scheme, so that
379 they require from a previous training stage.

380 The WCCD algorithm has been slightly modified to compute the energy
381 for all the pixels of the image instead of computing it at a patch level (the
382 same energy value was originally used within a 15×15 pixels patch), in
383 order to obtain finer classification results.

384 To perform the assessment, the original dataset was reduced to just con-

385 sider the images which contain corrosion. The resultant dataset, containing
 386 49 images, was evaluated using the five defect detectors, as well as for the
 387 WCCD algorithm. The ROC curves have been computed for the different
 388 detectors and are provided in Fig. 9.

389 As can be observed, the ROC curve for WCCD is comparable to the one
 390 obtained using the symmetry-based detector, but is considerable below the
 391 obtained using all the other defect detectors. The detector using the ORA
 392 combination operator is again the one which provides the best results.

393 In a second comparative assessment, we have used the defect detector
 394 presented in Bonnin-Pascual and Ortiz (2014a). This algorithm combines
 395 contrast and symmetry information through the Bayesian framework SUN
 396 (Zhang et al., 2008) to provide a saliency value for every pixel in the image.
 397 To be more precise, the saliency at a given point z is defined as:

$$S_z = \frac{1}{p(F = f_z)} p(F = f_z | C = 1), \quad (18)$$

398 where F represents the visual features associated to a point (contrast and/or
 399 symmetry), f_z represents the feature values observed at z , and C denotes
 400 whether a point belongs to the target class or not ($1 =$ defective area). Using
 401 this formulation, the saliency of a given point z decreases as the probability
 402 of features f_z is higher, and increases as the probability of f_z in defects
 403 increases. The Parzen windows method was applied once again to estimate
 404 those probabilities, using all the images of the dataset.

405 Notice that, despite both approaches use contrast and symmetry as fea-
 406 tures to describe the defective areas, the SUN-based detector requires from a
 407 training stage to estimate the probability distributions, and its feature com-
 408 bination is performed within a probabilistic formulation, while we propose
 409 three different combinations inspired by logical operators.

410 To perform the assessment, we have used the complete dataset. Three
 411 different configurations of the SUN-based detector have been considered: us-
 412 ing only contrast, using only symmetry and using both features. These three
 413 configuration have been evaluated through Leave-One-Out-Cross-Validation
 414 (Duda et al., 2000) and their corresponding ROC curves and AUC values have
 415 been computed. Figure 10 compares these results with the ones obtained for
 416 the corresponding three configurations of our framework: using only con-
 417 trast, using only symmetry and using both features combined through the
 418 ORA operator.

419 As can be observed, the results obtained with the defect detection frame-
420 work presented in this paper are very similar to the ones obtained using the
421 SUN framework. This indicates that a successful defect detection can be
422 attained using contrast and symmetry information without performing any
423 training stage, as the SUN-based detectors do.

424 In a fourth kind of experiments, we have checked the usability of the
425 defect detectors with images taken by the aerial robotic platform presented
426 in Bonnin-Pascual et al. (2015). Regarding vessel inspection, this platform
427 can be operated under *inspection mode*, what means constant and reduced
428 speed (if it is not hovering) while keeping the same distance and orientation
429 with regard to the front wall, to improve the image capture.

430 The aerial vehicle was flown in three different areas of a bulk-carrier: a
431 cargo hold, a top-side ballast tank, and the fore-peak tank. Three datasets
432 have been generated (one for each area) containing a total amount of 220
433 images. Ground-truth images has been manually generated as for previous
434 datasets. To perform the assessment, the performance of our five defect
435 detectors have been evaluated considering the three datasets both separately
436 and jointly:

- 437 • Figure 11 shows the ROC curves and AUC values obtained with the
438 five defect detectors when evaluating the cargo hold dataset. Images in
439 this dataset present very few defective areas so that most of the miss-
440 classifications correspond to false positives. In this conditions, all the
441 defect detectors present very high performance. The detectors which
442 combine contrast information present the best results, with AUC val-
443 ues above 0.95, while the symmetry-based detector performs slightly
444 worse, with an AUC around 0.9.
- 445 • Figures 12 and 13 show the results obtained for the datasets containing
446 images from the top-side and fore-peak ballast tanks. Images in these
447 datasets present many corroded areas which cover a considerable part
448 of the image. Unlike previous experiments, results show that symmetry
449 performs much better than contrast for these datasets (the AUC values
450 are around than 10 points higher). These interesting results indicate
451 that, in certain scenarios, defects can be detected thanks to its level
452 of symmetry, despite its value of contrast is not very discriminative.
453 The lower performance presented by contrast is probably due to the
454 LED that has been fitted in the aerial platform to enlighten the ins-
455 pected area inside the ballast tanks. The LED probably increases the

456 contrast level of many points in the structure (e.g. creating shadows),
457 increasing the number of false positives. Among the five detectors, the
458 OR combination (not the ORA) presents the best results for these two
459 datasets.

- 460 • Figure 14 presents the results obtained after evaluating all the images
461 of the three datasets jointly. With such an heterogeneous dataset, the
462 three detectors which combine contrast and symmetry perform consider-
463 ably better than the single-feature detectors, with AUC values that
464 exceed 0.82.

465 As way of example, Fig. 15 presents an image for each dataset, together
466 with its ground truth and the outputs provided by the five defect detectors.

467 In a last experiment, the vehicle was flown in front of a 2.5×4 m surface
468 containing corroded areas while its vision system was taking pictures at 10
469 Hz. The collected images were then processed by the image mosaicing algo-
470 rithm described in Garcia-Fidalgo et al. (2015), which managed to produce
471 the seamless composite shown in Fig. 16 (A). Finally, the mosaic was anal-
472 ysed using the five defect detectors which provided the defect maps shown in
473 Fig. 16 (C-G). Notice that the detector does not analyse the mosaic borders
474 since contrast and symmetry levels can not be successfully computed in these
475 areas. A ground truth image has been manually generated for the mosaic
476 (see Fig. 16 (B)) in order to check the quality of the defect maps. As can be
477 observed, lighter pixels in the defect maps, that is, those which are likelier
478 to correspond to defects according to our detectors, are indeed labelled in
479 white in the ground truth.

480 **5. Conclusions**

481 A novel algorithm for defect detection on vessel structures has been pre-
482 sented. This has been devised as a generic framework that can be configured
483 ad hoc, selecting the features (and the way to combine them) that pro-
484 vide a more successful classification of the defective and non-defective areas.
485 The detection framework can merge multi-scale information of the selected
486 features to increase the robustness of the detection against changes in the
487 distance to inspected area when collecting the images.

488 The selection of the features for our particular problem has been inspired
489 by the idea of conspicuity and taking into account the kind of defects that

490 appear in the metallic structures of vessels. The contrast in intensity, color
491 and orientation, and the isotropic symmetry have been the features selected.
492 Three different combinations of these features inspired by logical operators
493 have been also considered, in order to merge their information and provide
494 a better description of the defective situations.

495 The different defect detectors have provided good classification perfor-
496 mances, improving the results obtained with previous detectors. In compari-
497 son with them, the presented algorithm does not require from tuning a large
498 set of working parameters nor performing a previous training stage.

499 Regarding the feature set, the results obtained for the different datasets
500 indicate that contrast and symmetry complement each other, so that one can
501 provide the proper information to discriminate whether an area is defective
502 or not when the other feature maybe fails, and vice versa.

503 The usability of the proposed solution has been also proved using images
504 collected by a micro-aerial robotic platform devised for vessel inspection,
505 which has been flown in different areas inside a bulk carrier.

506 The experimental results have shown that the algorithm is also able to
507 successfully detect the defective situations in mosaics generated from these
508 images. During a vessel inspection campaign, the use of mosaics allows us
509 to extract more information about the state of the inspected surface since
510 defective areas are not split over multiple images.

511 Acknowledgements

512 This work is partially supported by FEDER funding, by project nr.
513 AAEE50/2015 (Direcció General d'Innovació i Recerca, Govern de les Illes
514 Balears), and by projects INCASS and ROBINS. The latter have received
515 research funding from the EU FP7 under GA 605200 and EU H2020 under
516 GA 779776. These publications reflect only the authors views and the Eu-
517 ropean Union is not liable for any use that may be made of the information
518 contained therein.

519 References

- 520 Avraham, T., Lindenbaum, M., 2010. Esaliency (Extended Saliency): Mean-
521 ingful Attention Using Stochastic Image Modeling. IEEE Transactions on
522 Pattern Analysis and Machine Intelligence 32 (4), 693–708.

- 523 Bonnin-Pascual, F., 2010. Detection of Cracks and Corrosion for Automated
524 Vessels Visual Inspection. Master's thesis, University of the Balearic
525 Islands.
- 526 URL {http://dmi.uib.es/~xbonnin/static/papers/mthesis_Bonnin2010.pdf}
- 528 Bonnin-Pascual, F., Ortiz, A., 2014a. A Probabilistic Approach for Defect
529 Detection Based on Saliency Mechanisms. In: IEEE International Conference
530 on Emerging Technologies and Factory Automation.
- 531 Bonnin-Pascual, F., Ortiz, A., 2014b. Corrosion Detection for Automated Vi-
532 sual Inspection. In: Aliofkhazraei, D. M. (Ed.), Developments in Corrosion
533 Protection. InTech, Ch. 25, pp. 619–632.
- 534 Bonnin-Pascual, F., Ortiz, A., Garcia-Fidalgo, E., Company, J. P., 2015. A
535 Micro-Aerial Platform for Vessel Visual Inspection based on Supervised
536 Autonomy. In: IEEE/RSJ International Conference on Intelligent Robots
537 and Systems. pp. 46–52.
- 538 Borji, A., Ahmadabadi, M. N., Araabi, B. N., 2011. Cost-sensitive Learn-
539 ing of Top-Down Modulation for Attentional Control. Machine Vision and
540 Applications 22 (1), 61–76.
- 541 Borji, A., Itti, L., 2013. State-of-the-Art in Visual Attention Modeling. IEEE
542 Transactions on Pattern Analysis and Machine Intelligence 35 (1), 185–207.
- 543 Chin, R. T., Harlow, C. A., 1982. Automated Visual Inspection: A Survey.
544 IEEE Transactions on Pattern Analysis and Machine Intelligence 4 (6),
545 557–573.
- 546 Duda, R. O., Hart, P. E., Stork, D. G., 2000. Pattern Classification, 2nd
547 Edition. Wiley Interscience.
- 548 Eich, M., Bonnin-Pascual, F., Garcia-Fidalgo, E., Ortiz, A., Bruzzone, G.,
549 Koveos, Y., Kirchner, F., 2014. A Robot Application to Marine Vessel
550 Inspection. Journal of Field Robotics 31 (2), 319–341.
- 551 Fawcett, T., 2006. An Introduction to ROC Analysis. Pattern Recognition
552 Letters 27 (8), 861–874.

- 553 Garcia-Fidalgo, E., Ortiz, A., Bonnin-Pascual, F., Company, J. P., 2015.
554 A Mosaicing Approach for Vessel Visual Inspection using a Micro-Aerial
555 Vehicle. In: IEEE/RSJ International Conference on Intelligent Robots and
556 Systems.
- 557 Itti, L., Koch, C., Niebur, E., nov 1998. A Model of Saliency-based Visual At-
558 tention for Rapid Scene Analysis. *IEEE Transactions on Pattern Analysis*
559 and Machine Intelligence
- 560 20 (11), 1254 –1259.
- 561 Jahanshahi, M. R., Kelly, J. S., Masri, S. F., Sukhatme, G. S., 2009. A
562 Survey and Evaluation of Promising Approaches for Automatic Image-
563 based Defect Detection of Bridge Structures. *Structure and Infrastructure*
564 Engineering
- 565 5 (6), 455–486.
- 566 Koch, C., Ullman, S., 1985. Shifts in Selective Visual Attention: Towards
567 the Underlying Neural Circuitry. *Human Neurobiology*
- 568 4 (4), 219–227.
- 569 Kootstra, G., Nederveen, A., Boer, B. D., 2008. Paying Attention to Sym-
570 metry. In: *British Machine Vision Conference*. BMVA Press, pp. 111.1–
571 111.10.
- 572 Kootstra, G., Schomaker, L., 2009. Prediction of Human Eye Fixations Using
573 Symmetry. In: *Annual Conference of the Cognitive Science Society*. pp.
574 56–61.
- 575 Li, J., Tian, Y., Huang, T., Gao, W., 2010. Probabilistic Multi-task Learning
576 for Visual Saliency Estimation in Video. *International Journal of Computer*
577 Vision
- 578 90 (2), 150–165.
- 579 Malamas, E. N., Petrakis, E. G. M., Zervakis, M., Petit, L., Legat, J.-D.,
580 2003. A Survey on Industrial Vision Systems, Applications and Tools. *Im-*
581 *age and Vision Computing*
- 582 21, 171–188.
- 583 Mumtaz, M., Masoor, A. B., Masood, H., 2010. A new approach to aircraft
584 surface inspection based on directional energies of texture. In: *Inter-
585 national Conference on Pattern Recognition*. pp. 4404–4407.
- 586 Newman, T. S., 1995. A Survey of Automated Visual Inspection. *Computer*
587 *Vision and Image Understanding*
- 588 61 (2), 321–262.

- 583 Ozog, P., Eustice, R. M., 2015. Identifying Structural Anomalies in Image
584 Reconstructions of Underwater Ship Hulls. In: IEEE/MTS OCEANS Con-
585 ference and Exhibition.
- 586 Siegel, M., Gunatilake, P., 1998. Remote enhanced visual inspection of air-
587 craft by a mobile robot. In: IEEE International Workshop on Emergent
588 Technologies, Intelligent Measurement and Virtual.
- 589 Theodoridis, S., Koutroumbas, K., 2006. Pattern Recognition, 3rd Edition.
590 Academic Press.
- 591 Wolfe, J. M., 2007. Integrated Models of Cognitive Systems. In: Gray, W. D.
592 (Ed.), Guided search 4.0. Oxford University Press New York, NY, Ch. 8,
593 pp. 99–119.
- 594 Xie, X., 2008. A Review of Recent Advances in Surface Defect Detection
595 Using Texture Analysis Techniques. Electronic Letters on Computer Vision
596 and Image Analysis 7 (3), 1–22.
- 597 Yamaguchi, T., Hashimoto, S., 2010. Fast Crack Detection Method for Large-
598 size Concrete Surface Images Using Percolation-based Image Processing.
599 Machine Vision and Applications 21 (5), 797–809.
- 600 Zhang, L., Qiu, B., Yu, X., Xu, J., 2015. Multi-scale Hybrid Saliency Analysis
601 for Region of Interest Detection in Very High Resolution Remote Sensing
602 Images. Image and Vision Computing 35, 1–13.
- 603 Zhang, L., Tong, M. H., Marks, T. K., Shan, H., Cottrell, G. W., 2008. SUN:
604 A Bayesian Framework for Saliency Using Natural Statistics. Journal of
605 Vision 8 (7), 1–20.

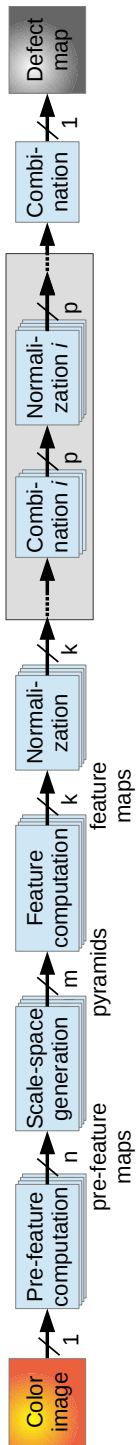


Figure 1: Generic framework for defect detection.

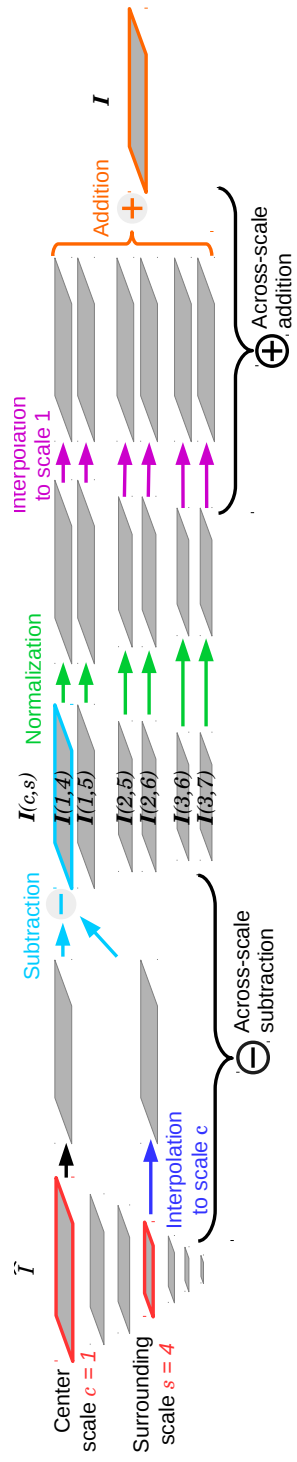


Figure 2: Illustration of feature map computation: case of intensity-contrast map.

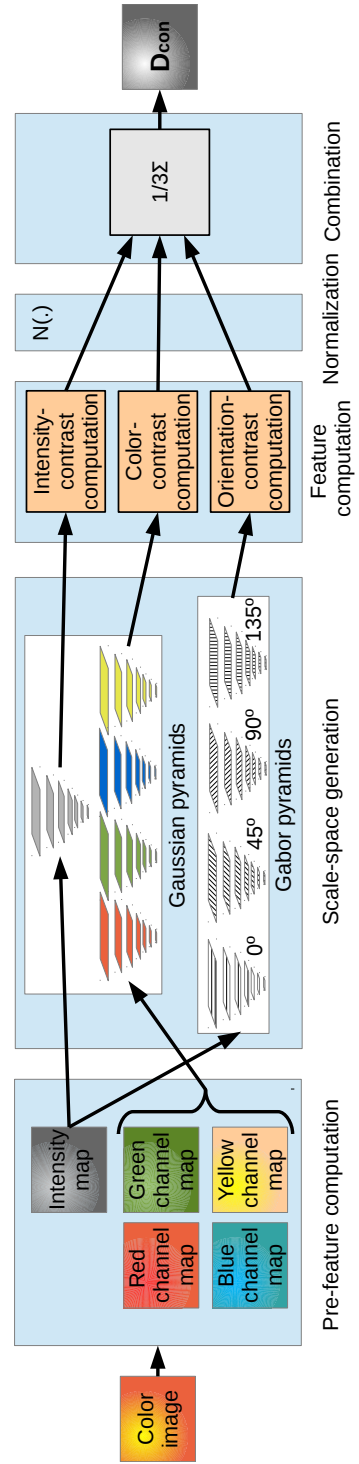


Figure 3: Implementation of the contrast-based defect detector using our generic framework.

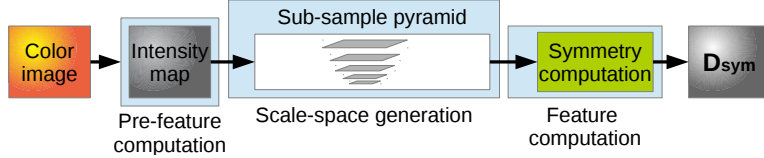


Figure 4: Implementation of the symmetry-based defect detector using our generic framework.

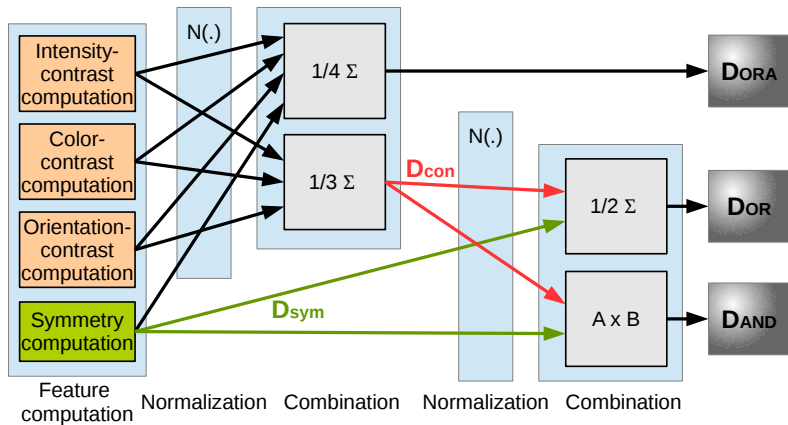


Figure 5: Set up of the normalization and combination stages for the three versions of the defect detector merging contrast and symmetry information.

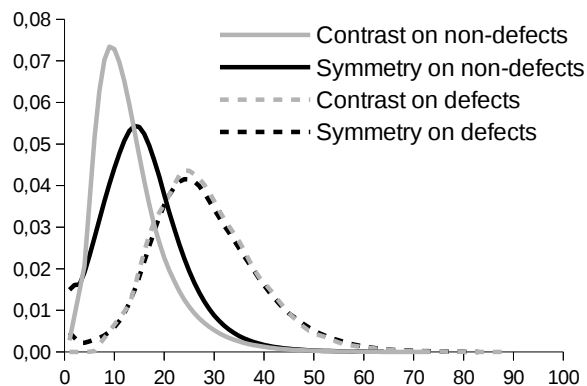


Figure 6: PDFs obtained for contrast and symmetry features.



Figure 7: Test images with their associated ground truth and defect maps. A: original image. B: ground truth. C and D: respectively, defect maps obtained using contrast and symmetry. E, F and G: respectively, defect maps obtained from the OR, AND and ORA combinations.

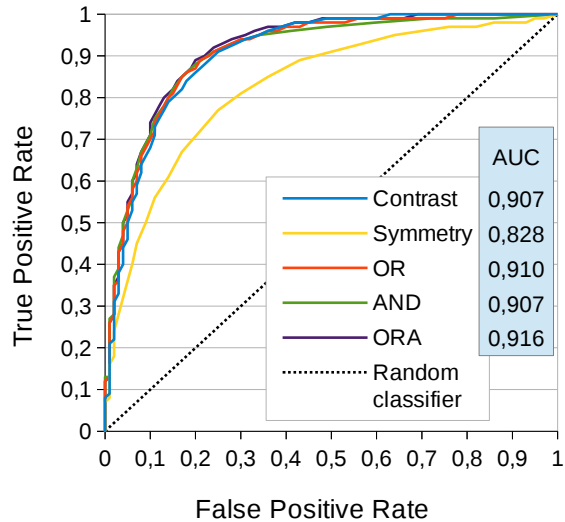


Figure 8: ROC curves and AUC values obtained for the five defect detectors.

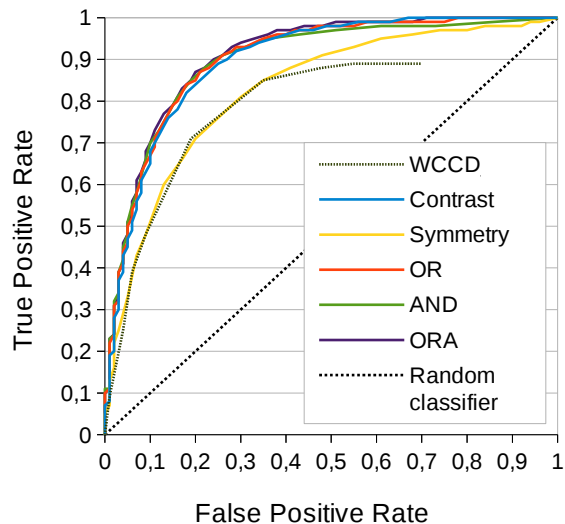


Figure 9: Comparison between our defect detectors and WCCD algorithm, when looking for corroded areas.

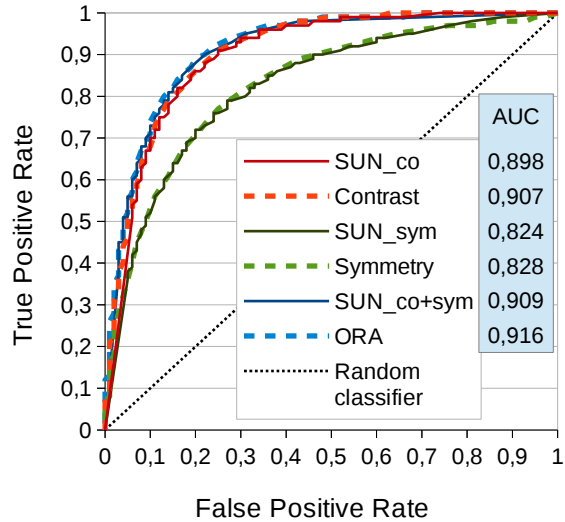


Figure 10: Comparison between our defect detectors and the SUN-based ones.

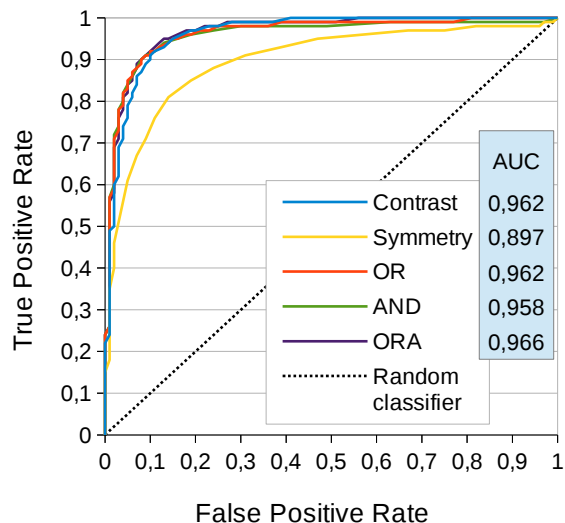


Figure 11: ROC curves and AUC values obtained for the five detectors evaluating images taken from a cargo hold inside a bulk carrier.

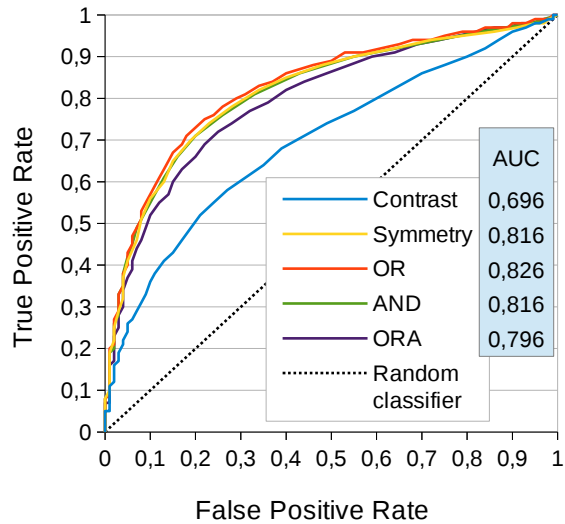


Figure 12: ROC curves and AUC values obtained for the five detectors evaluating images taken from a top-side ballast tank inside a bulk carrier.

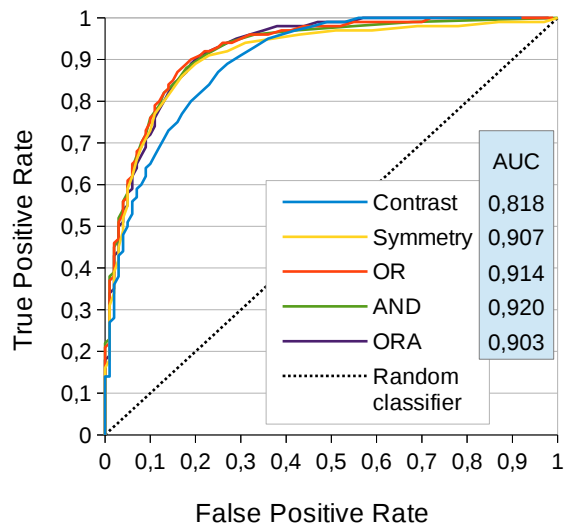


Figure 13: ROC curves and AUC values obtained for the five detectors evaluating images taken from the fore-peak tank of a bulk carrier.

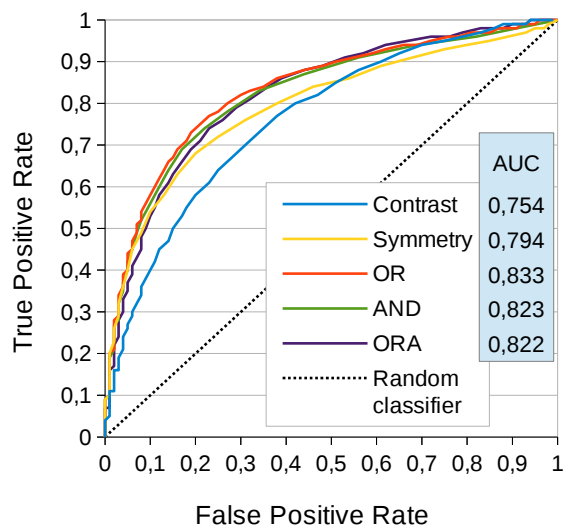


Figure 14: ROC curves and AUC values obtained for the five detectors evaluating the images taken from three different spaces inside a bulk carrier: a cargo hold, a top-side ballast tank and the fore-peak tank.

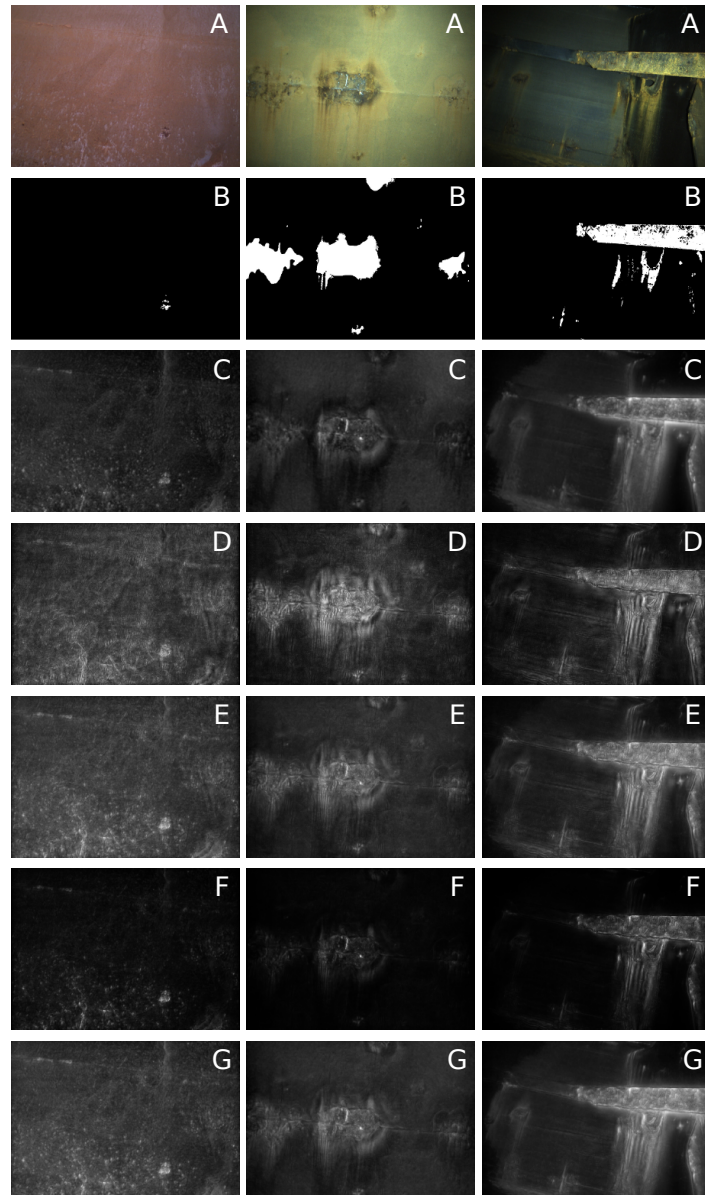


Figure 15: Results obtained for three images taken inside the bulk carrier: a cargo hold (left), a top-side ballast tank (middle), and the fore-peak tank (right). A: original image. B: ground truth. C and D: respectively, defect maps obtained using contrast and symmetry. E, F and G: respectively, defect maps obtained from the OR, AND and ORA combinations.

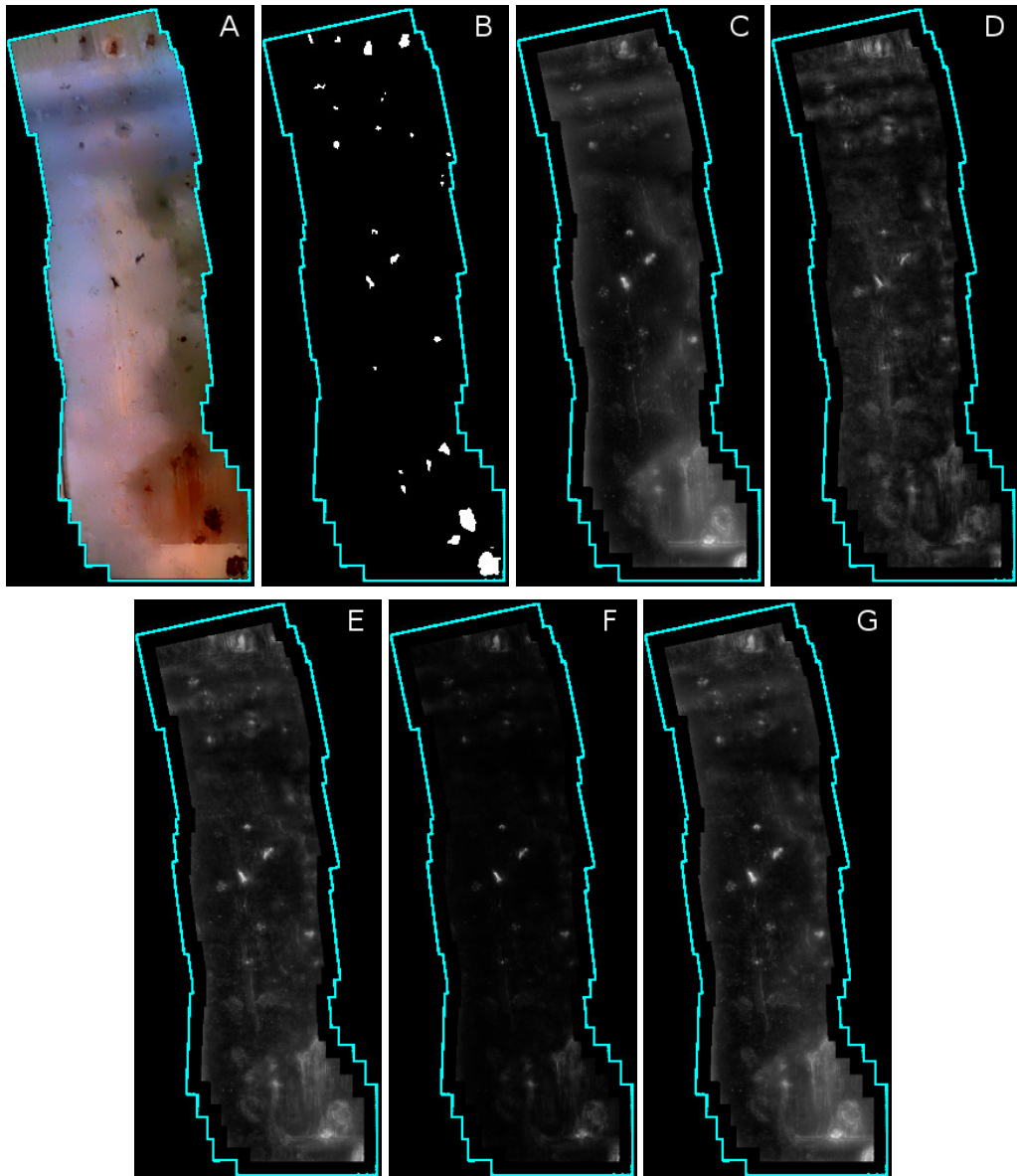


Figure 16: Detection results when inspecting an image mosaic. A: mosaic built from images collected by the aerial vehicle. B: ground truth image manually generated. C and D: respectively, defect maps obtained using contrast and symmetry. E, F and G: respectively, defect maps obtained from the OR, AND and ORA combinations. In defect maps, lighter pixels are likelier to correspond to defects (mosaic borders are not analysed).